




High-sensitivity and low-volume-based piezoelectric MEMS acceleration sensor using *PiezoMUMPs*

Priyabrata Biswal^{1,*} , Mithlesh Kumar², Sougata Kumar Kar¹, and Banibrata Mukherjee³

¹ Department of ECE, NIT Rourkela, Rourkela, Odisha 769008, India

² Honeywell Automation India Limited, Bangalore, Karnataka 560103, India

³ Advanced Technology Development Centre, IIT Kharagpur, Kharagpur, West Bengal 721302, India

Received: 20 July 2023

Accepted: 24 October 2023

Published online:
16 November 2023

© The Author(s), under exclusive licence to Springer Science+Business Media, LLC, part of Springer Nature, 2023

ABSTRACT

The piezoelectric-based accelerometer gains popularity due to its capability to produce direct electrical output. In this work, two new meander architecture-based high-performance piezoelectric accelerometers have been proposed and their performance characteristics are extensively analyzed. The meander-based accelerometers are designed using *PiezoMUMPs* fabrication technology which uses $0.5 \mu\text{m}$ *AlN* piezo layer. The designed structures are having overall area of $1.08 \text{ mm} \times 1.8 \text{ mm}$ and $1.96 \text{ mm} \times 1.8 \text{ mm}$ with voltage sensitivity of 3.92 V/g and 1.8 V/g , respectively, in resonant region. The proposed meander architecture utilizes low volume and exhibits improved dynamic characteristics in terms of higher voltage sensitivity, lower-resonant frequencies, and better structural stability with respect to reported literature. Further, the energy-harvesting aspects for these meander-based structures have been explored, and the harvested power of the proposed structure is higher than the conventional structure.

1 Introduction

The vibration measurement has been explored in different applications such as structural health monitoring, fault detection in different industrial equipment, automobile sectors, and robot-operated industrial operations to counter any undesired incidents. Nowadays, the inertial sensors like accelerometer, gyroscope, and compact vibration sensors are used in different internet of things (IoT) nodes like buildings, tunnels, vehicles for accident detection, railway tracks, etc. With the increase in technological advancement,

the design and development of vibration sensors have drawn attention of researchers to enhance the performance of these sensors in terms of high efficiency, greater sensitivity, low cost, and high bandwidth. The accelerometers/vibration sensors operate on different transduction techniques such as piezoresistive, electrostatic, piezoelectric, optical, and electromagnetic. In case of piezoresistive and electrostatic-based accelerometers, external power supply is required for their operation to provide electrical output [1–4]. However, the piezoelectric type vibration sensor can directly produce electrical output corresponding to a given

Mithlesh Kumar, Sougata Kumar Kar, and Banibrata Mukherjee have contributed equally to this work.

Address correspondence to E-mail: priya.nitrkl2017@gmail.com; 517ec6006@nitrkl.ac.in

E-mail Addresses: mithlesh.ece@gmail.com; kars@nitrkl.ac.in; banibratam@atdc.iitkgp.ac.in

vibration based on its inherent piezoelectric effect. Due to self-generating capability of piezoelectric materials, different low power sensors can be implemented as self-powered sensor and one such emerging area of interest is piezoelectric nanogenerator. Piezoelectric nanogenerators exhibit potential for different sensors such as mass sensor, piezoresistive vibration sensor, gas sensor, humidity sensor, formaldehyde sensor, and ammonia sensor [5, 6]. Zhang et. al experimentally demonstrated a piezoelectric nanogenerator that harvests energy from the human body using vibration energy and molybdenum disulfide-based piezo nanogenerator is utilized for powering ammonia sensor [7]. A piezoelectric accelerometer utilizing piezoelectric material *AlN* of $1\ \mu\text{m}$ thickness is fabricated by Shin et. al, and it exhibits resonant frequency of $427.1\ \text{kHz}$ [8]. Wang group investigated the usability of Molybdenum Diselenide-based piezo nanogenerator for flexible electronics application such as humidity-sensing application and the proposed piezoelectric generator produces $35\ \text{mV}$ as peak output voltage [9]. Piezoelectric inertial sensors can be fabricated using either customized MEMS or piezoelectric multi-user MEMS processes (*PiezoMUMPs*). The change in environmental policies with respect to different countries in the global scenario insists researchers to work on biocompatible materials and/or devices. The biocompatible piezoelectric materials such as aluminum nitride (*AlN*) or Zinc Oxide (*ZnO*) are widely utilized by researchers for development of piezo devices. A *ZnO/MXene*-based piezo nanogenerator is explored to demonstrate self-powered capability to power the formaldehyde gas sensor by Zhang group [10] and the demonstrated piezo nanogenerator generated output power of $15.4\ \text{nW}$ at the resistance of $2\ \text{M}\Omega$. With increase in demand of low-cost compact size of sensors, the micro-electro mechanical systems (MEMS) technology is accepting the challenge by taking care of parameters such as feature size, ease of operation, sensitivity, and efficiency of these sensors [11, 12].

Chen et. al designed a ring-type microaccelerometer using customized MEMS fabrication process for application of vibration measurement, which is capable of producing $141.10\ \text{mV}$ with application of $10\ \text{g}$ acceleration [13]. In their work, the proposed vibration sensor used $1\ \mu\text{m}$ aluminum nitride (*AlN*) as piezoelectric material on silicon (*Si*) substrate and operated at resonant frequency of $7.2\ \text{kHz}$ [13]. Liu et. al have designed a folded beam-based piezoelectric accelerometer using customized MEMS process, which gives

charge sensitivity of $3.35\ \text{pC/g}$ in z-axis and $0.66\ \text{pC/g}$ in y-axis. Furthermore, the overall area is $17\ \text{mm} \times 9\ \text{mm}$, which consists of a large proof mass having dimension of $7\ \text{mm} \times 3.5\ \text{mm}$ and the resonant frequency of the piezoelectric accelerometer is $11.7\ \text{kHz}$ [14]. A four beam-based MEMS piezoelectric accelerometer has been reported by Gupta et. al, where the overall area of the design is $1.6\ \text{mm} \times 1.6\ \text{mm}$. In their work, the accelerometer has been designed using $0.85\ \mu\text{m}$ *AlN* piezo layer, and the resonant frequency is found to be $5.19\ \text{kHz}$ [15]. A tuning fork-based piezoelectric resonant accelerometer having overall area of $1.375\ \text{mm} \times 1.728\ \text{mm}$ using customized MEMS process has been fabricated by Yang et. al [16]. The overall thickness and resonant frequency of their structure are $2.05\ \mu\text{m}$ and $24.66\ \text{kHz}$, respectively. They have utilized *AlN* as piezoelectric material, and relative sensitivity of the fabricated accelerometer is $8.53\ \text{Hz/g}$. Apart from conventional electrode placement in piezoelectric accelerometer, researchers are also exploring on interdigitated electrode mechanism. A *PLZT* ($(\text{Pb}, \text{La})(\text{Zr}, \text{Ti})\text{O}_3$) film based on piezoelectric MEMS accelerometer has been experimentally demonstrated by Shen et. al for vibration-sensing and monitoring applications [17]. In their work, the fundamental resonant frequency of the proposed accelerometer is about $8.26\ \text{kHz}$, and the charge sensitivity at $1\ \text{kHz}$ is found to be $0.04\ \text{pC/g}$. A screen-printed piezoelectric accelerometer using *PZT* (lead zirconate titanate) has been fabricated by Hindrichsen et. al, and the reported accelerometer exhibits first-mode resonance frequency of $11\ \text{kHz}$ [18]. In their work, the designed accelerometer gives voltage sensitivity of $0.31\ \text{mV/g}$ in out-of-plane direction and $0.062\ \text{mV/g}$ in in-plane direction.

A $6.3\ \text{mm} \times 5.6\ \text{mm}$ piezoelectric vibration sensor has been fabricated in active die area of $9.65\ \text{mm} \times 9.65\ \text{mm}$ and experimentally demonstrated by Sinatra et. al [19]. The meander structure is capable of generating $2.3\ \text{mV}$ at acceleration of $0.062\ \text{g}$ with resonant frequency of $20\ \text{Hz}$ [19]. However, such conventional meander architecture uses large volume. A circular membrane-shaped piezoelectric vibration sensor has been designed with die area of $2.3\ \text{mm} \times 2.3\ \text{mm}$ as reported in [20]. The sensor produces voltage of $355\ \text{mV/g}$ at resonant frequency of about $12.5\ \text{kHz}$ (open-circuit sensitivity $440\ \mu\text{V/g}$). Although the sensing voltage is significant with the proposed design, but the application is limited to very high-frequency-operating conditions due to high resonant frequency. Table 1 represents a brief summary

Table 1 Review of reported literatures

Ref.	Architecture	Piezo material	Overall area (mm^2)	Fabrication process	Resonant frequency	Sensitivity
[19]	Meander	AlN	35.28	PiezoMUMPs	20 Hz	0.0038V/(m/s^2)
[20]	Membrane	AlN	5.29	PiezoMUMPs	10 kHz	350 mV/g
[13]	Ring	AlN	63.61	Custom	7.2 kHz	14.3 mV/g
[21]	DETF	AlN	3.2	PiezoMUMPs	141 kHz	28.4 Hz/g
[22]	T-Shape	AlN	0.31	Custom	16.10 kHz	1.11 Hz/g
[23]	Cantilever	PZT	49	Custom	3.04 kHz	149.8 mV/g

of reported literature, which have worked on different acceleration or vibration sensor.

The reported work in the literature uses high volume and exhibits low sensitivity in terms of output voltage, charge sensitivity. Therefore, our work is focused on reducing the overall volume and increasing the sensitivity of the sensor. We have proposed meander-type vibration/acceleration sensor, which uses folded springs for sake of lower-resonant frequency. Also, the meander architecture provides high sensitivity due to its unique design topology. The parameters such as resonant frequency, piezoelectric material, area, charge sensitivity, and voltage sensitivity of the piezoelectric acceleration sensor has been discussed with simulation results. The current work provides two types of design for the piezoelectric acceleration sensor, namely half-meander and meander, which are capable of measuring acceleration in both the out-of-plane as well as in-plane direction of measurement. Furthermore, the energy-harvesting prospective for the designed proposed structure has been discussed. The details about the material used and methods adopted are presented in Sect. 2, where the process technology as well as different configurations of MEMS sensor are discussed. The extensive simulation studies, results, and discussions, comparison with related literature, and layout of the proposed meander sensor design are presented in Sect. 3, and conclusion is summarized in Sect. 4 giving insight on the scope of the proposed acceleration sensor in acceleration/vibration monitoring as well as measuring applications.

2 Materials and methods

The vibration sensor has been designed using PiezoMUMPs technology and the intended application includes in-plane as well as out-of-plane vibration measurement. The vibration sensor is self-generating

type due to utilization of piezoelectric material as vibration-sensing material. The *PiezoMUMPs* technology followed by the design of different sensor configuration such as half-meander and meander architecture is presented in the following.

2.1 PiezoMUMPs technology

The *PiezoMUMPs* process came into effective in the year of 2013 dedicated for fabrication of piezoelectric devices. The process uses five-mask level process, which uses a fixed 0.5 μm AlN layer on SOIMUMPs process. The *PiezoMUMPs* process uses PADOXIDE layer (0.2 μm), piezoelectric material layer (0.5 μm), PADMETAL layer (1.02 μm), Silicon (10 μm), and Oxide layer (1 μm) on the silicon substrate of 400 μm thickness. The five-mask level process starts with PADOXIDE and end with TRENCH as last [24]. The rules and guidelines of the *PiezoMUMPs* process for designing piezoelectric sensors as well as energy harvesters can be found further in [25, 26].

2.2 Design of MEMS acceleration sensor

Figure 1 represents the topology of the proposed inertial sensor. Figure 1a and b represents conventional structure and proposed half-meander structure, respectively. Similarly, Fig. 1c and d illustrates another type of conventional architecture and the proposed full meander structure, respectively. The dimension of both the meander structures is illustrated in Table 2 and the detail working principle of these structures are discussed briefly in Sects. 2.2.2 and 2.2.3. In the proposed sensor designs, the folded spring structure reduces stiffness substantially in comparison to conventional cantilever type springs, thereby reducing the resonant frequency of the proposed sensor designs. The sensors are designed considering applications of

Table 2 Dimension of vibration sensor

Details		Dimension in μm
Proof mass	Length, L_m	1200
	Width, W_m	200
	thickness, h_m	400
Spring	Length, L_s	800
	Width, W_s	100
	Gap between folds, W_g	30
	Gap between parallel spring, g_{ps}	200
Anchor section	Length, L_{ref}	100
	Width, W_{ref}	50
Structure layer	Thickness, t_s	10

vibration/acceleration measurement in both out-of-plane as well as in-plane direction.

2.2.1 Conventional configuration

The stiffness for conventional structure can be derived using Castigliano’s theorem by considering unit load applied to the beam. The spring constant for the single beam can be found as $k_{beam} = 12EI_n/L^3$, where E , L , I_n are Young’s modulus, length of the beam, and moment of inertia and n can be x-direction, y-direction, and z-direction. The stiffness for the conventional-I can be derived as follows:

The stiffness for the conventional-I structure is two times of k_{beam} . The spring constant along the x-direction, y-direction, and z-direction can be denoted as k_{xx} , k_{yy} , and k_{zz} respectively and are given in (1), (2), and (3) respectively, where t refers to thickness of beam and w refers to width of the beam.

$$k_{xx} = \frac{2 \times 12EI_z}{L^3} = \frac{2 \times Etw^3}{L^3} \tag{1}$$

$$k_{yy} = \frac{2 \times Etw}{L} \tag{2}$$

$$k_{zz} = \frac{2 \times 12EI_x}{L^3} = \frac{2 \times Ewt^3}{L^3} \tag{3}$$

Similarly, the stiffness for the conventional-II structure is four times of beam stiffness k_{beam} and are illustrated as follows:

$$k_{xx} = \frac{4 \times 12EI_z}{L^3} = \frac{4 \times Etw^3}{L^3} \tag{4}$$

$$k_{yy} = \frac{4 \times Etw}{L} \tag{5}$$

$$k_{zz} = \frac{4 \times 12EI_x}{L^3} = \frac{4 \times Ewt^3}{L^3} \tag{6}$$

2.2.2 Half-meander configuration

The half-meander structure and its corresponding conventional structure (conventional-I) are presented in Fig. 1b and a, respectively. The overall dimension of conventional structure is $1080 \mu\text{m} \times 1200 \mu\text{m}$. The half-meander architecture consists of three-folded springs with fixed-free configuration, where the proof mass of area $1 \text{ mm} \times 0.2 \text{ mm}$ has been used as illustrated in Fig. 1a. The overall area of half-meander design is $1080 \mu\text{m} \times 1800 \mu\text{m}$, which is lesser than the design reported by Sinatra et. al [19]. Moreover, the structure uses a secondary mass in addition to primary mass which leads to large volume requirement. In the half-meander design, the piezo material *AlN* having thickness as per *Piezo-MUMPs* process has been deposited over the spring region except proof mass section. The tip mass can be calculated by considering the density of silicon 2329 kg/m^3 and is found to be 0.223 mg . The two corrugated springs are connected parallel to each other, which provides structural stability as well as resistant to unnecessary bending due to large proof mass.

With the application of external force in terms of acceleration in either of the out-of-plane direction (thickness direction), the two parallel springs experience with the tensile stress/strain, thereby the piezoelectric material on the silicon structural layer ($10 \mu\text{m}$) generates voltages at the output terminal of the sensor, which makes it self-generating sensor. When the force is applied in in-plane direction (either of mass width direction), the stress/strain behavior of the meander beam changes and it gives the output voltage. The half-meander accelerometer can be analyzed by means of spring-mass-damper system, which is governed by the following equation:

$$m_{end}\ddot{x}(t) + d_c\dot{x}(t) + k_{eqv}x(t) = ASin\omega t = F_1(t) \tag{7}$$

where A is magnitude of acceleration, ω is angular frequency, m_{end} , d_c , and k_{eqv} are end mass, damping constant, and equivalent stiffness, respectively. The

spring-mass-damper equivalent for the half-meander system is shown in Fig. 2a, and therefore, the equation (7) can be modified to (8) as shown in below:

$$m_{end}\ddot{x}_1(t) + (d_c)\dot{x}_1(t) + (k_1 + k_2)x_1 = F_1(t) \tag{8}$$

where d_c and k_{eqv} are represented as $(d_1 + d_2)$ and $(k_1 + k_2)$, respectively. The Castigliano theorem can be explored here to find out the stiffness for half-meander structure by considering total strain energy of the meander spring [27]. The stiffness for the half-meander structure in x-direction is given as (9).

$$k_{xx} = \frac{2 \times 12EI_{w_b}}{l_a^2 n [(r + w_b)n^2 - 3w_b n + 2w_b]} \tag{9}$$

where l_a , I_{w_b} , w_b and n refers to length of meander, inertia about width of meander, width of meander, and number of meanders. With reference to Fig. 1b, l_a , w_b , and I_{w_b} can be expressed as $l_a = (2 \times w_s) + w_g$, $w_b = l_s - l_g$, and $I_{w_b} = tw_s^3/12$, respectively. The inertia ratio factor r can be represented as $r = (I_{w_b} \times l_a) / (tl_g^3/12)$. Similarly, the stiffness of the half-meander structure in y-direction can be expressed as follows:

$$k_{yy} = \frac{2 \times 12EI_{w_b} [rn + w_b n - w_b]}{w_b^2 (n - 1) [(3r^2 + 4rw_b + w_b^2)n + 3r^2 w_b^2]} \tag{10}$$

Table 3 Stiffness of proposed structures

Structure	Stiffness	
	Analytical	FEM
Conventional I	$k_{xx} = 6.56 \text{ kN/m}$	$k_{xx} = 5.41 \text{ kN/m}$
	$k_{yy} = 4.2 \times 10^5 \text{ N/m}$	$k_{yy} = 4.4 \times 10^5 \text{ N/m}$
	$k_{zz} = 18.04 \text{ N/m}$	$k_{zz} = 20.62 \text{ N/m}$
Conventional II	$k_{xx} = 13.12 \text{ kN/m}$	$k_{xx} = 13.35 \text{ kN/m}$
	$k_{yy} = 8.4 \times 10^5 \text{ N/m}$	$k_{yy} = 8.83 \times 10^5 \text{ N/m}$
	$k_{zz} = 144.70 \text{ N/m}$	$k_{zz} = 170.62 \text{ N/m}$
Half-Meander	$k_{xx} = 1.60 \text{ kN/m}$	$k_{xx} = 1.55 \text{ kN/m}$
	$k_{yy} = 3.29 \text{ kN/m}$	$k_{yy} = 3.80 \text{ kN/m}$
Meander	$k_{xx} = 3.20 \text{ kN/m}$	$k_{xx} = 3.28 \text{ kN/m}$
	$k_{yy} = 6.59 \text{ kN/m}$	$k_{yy} = 7.80 \text{ kN/m}$

2.2.3 Meander configuration

We have proposed another design, named meander architecture by modifying the half-meander design. Another set of folded springs has been added to the proof mass end in the half-meander design, to form the meander configuration and is shown in Fig. 1d. The corresponding conventional architecture with respect to meander architecture is as shown in Fig. 1c, and its overall dimension is $1960 \mu\text{m} \times 1200 \mu\text{m}$. The dimension of proof mass, spring, and anchor region are same as that of half-meander design and is given in Table 2. The overall area of the meander design is $1960 \mu\text{m} \times 1800 \mu\text{m}$, which is occupying very less volume. The modeling of this meander design can be done by using spring-mass-damper system as illustrated in Fig. 2b and the equation is presented in (11).

$$m_{proof}\ddot{x}_1(t) + (d_{eqv})\dot{x}_1(t) + (k_{eqvt})x_1(t) = F_1(t) \tag{11}$$

where d_{eqv} referred to as damping constant and is given by $d_3 + d_4 + d_5 + d_6$. The equivalent stiffness k_{eqvt} is given by $k_3 + k_4 + k_5 + k_6$. Here, m_{proof} refers to end mass of the meander sensor, respectively. The Castigliano theorem can be utilized to find the stiffness for the meander structure. The meander structure consists of four-meander spring. So, the equivalent stiffness for the single-meander beam has been computed, and then it is multiplied by four to get the resultant stiffness in specified direction. The k_{xx} and k_{yy} are represented in (12) and (13), respectively.

$$k_{xx} = \frac{4 \times 12EI_{w_b}}{l_a^2 n [(r + w_b)n^2 - 3w_b n + 2w_b]} \tag{12}$$

$$k_{yy} = \frac{4 \times 12EI_{w_b} [rn + w_b n - w_b]}{w_b^2 (n - 1) [(3r^2 + 4rw_b + w_b^2)n + 3r^2 w_b^2]} \tag{13}$$

With the application of external forces in the in-plane direction, the two springs on the top side of proof mass (as shown in Fig. 1b) experience compressive forces and two springs on the bottom side of the proof mass experience tensile forces. In this case, the change in stress/strain along both side of masses determines the charge generation capacity of the piezo device. Similarly, the change in stress/strain profile can be analyzed with application of external acceleration in either side of out-of-plane direction (along the thickness direction of proof mass). The simulation studies

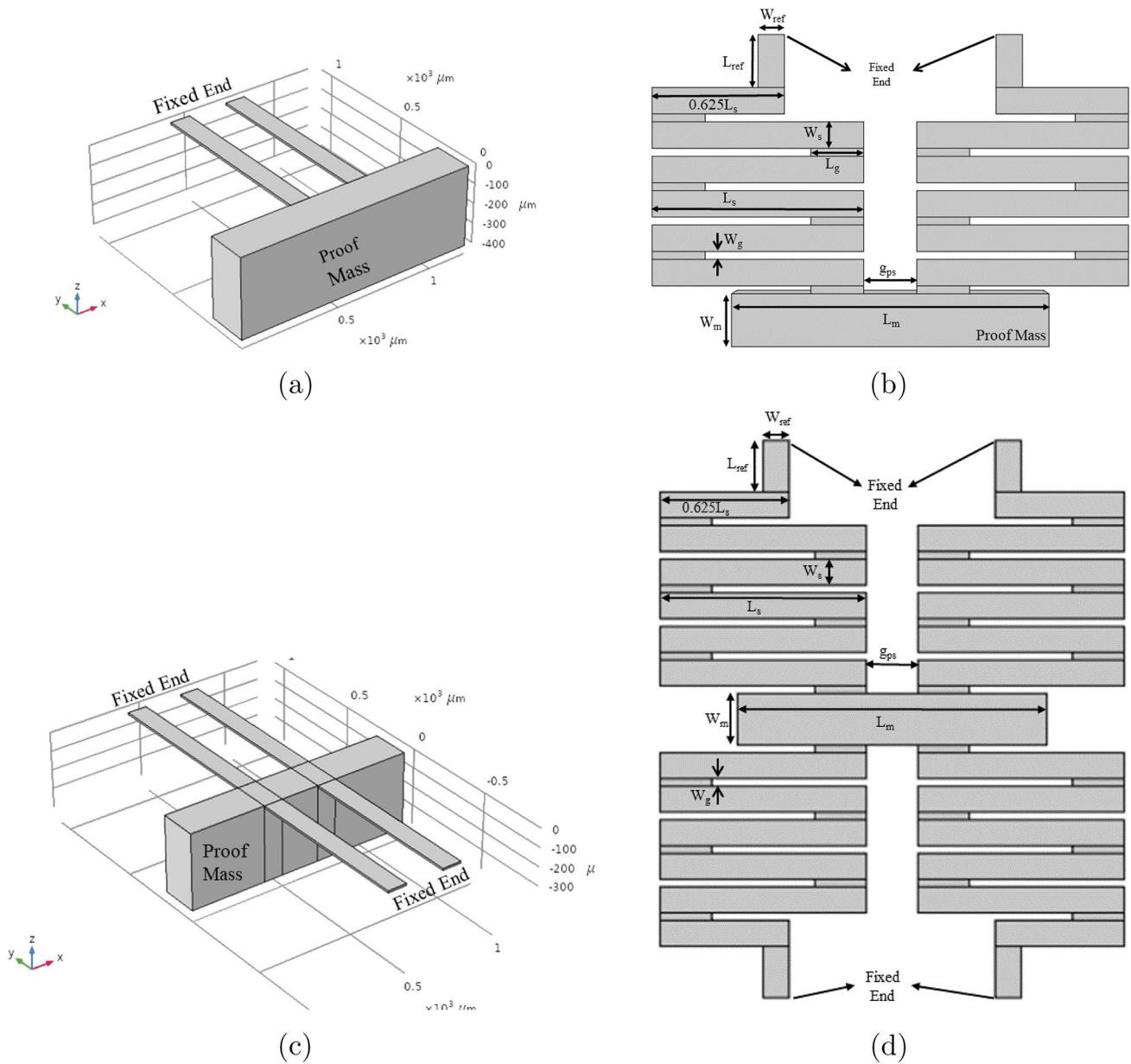


Fig. 1 Proposed acceleration sensor: **a** Conventional I, **b** top view of half-meander, **c** Conventional II, and **d** top view of meander

and layout of the proposed sensor have been presented in Sects. 3.2, 3.3, and 3.4, respectively.

3 Results and discussion

The meander design of the accelerometers has been simulated in finite-element analysis technique-based software COMSOL Multiphysics. Different domain

studies, like MEMS module, structural mechanics module, electrostatic module, and electrical circuit module have been utilized to characterize the performance of both half-meander and meander-type designs as presented in Fig. 1. The characteristics such as modes of vibration in terms of eigen frequency, von Mises stress distribution, and principal strain profile have been discussed in stationary study of Sect. 3.2. The frequency-domain analysis has been carried out for the sensor as well as harvester prospective and detail characteristics such as voltage sensitivity, charge

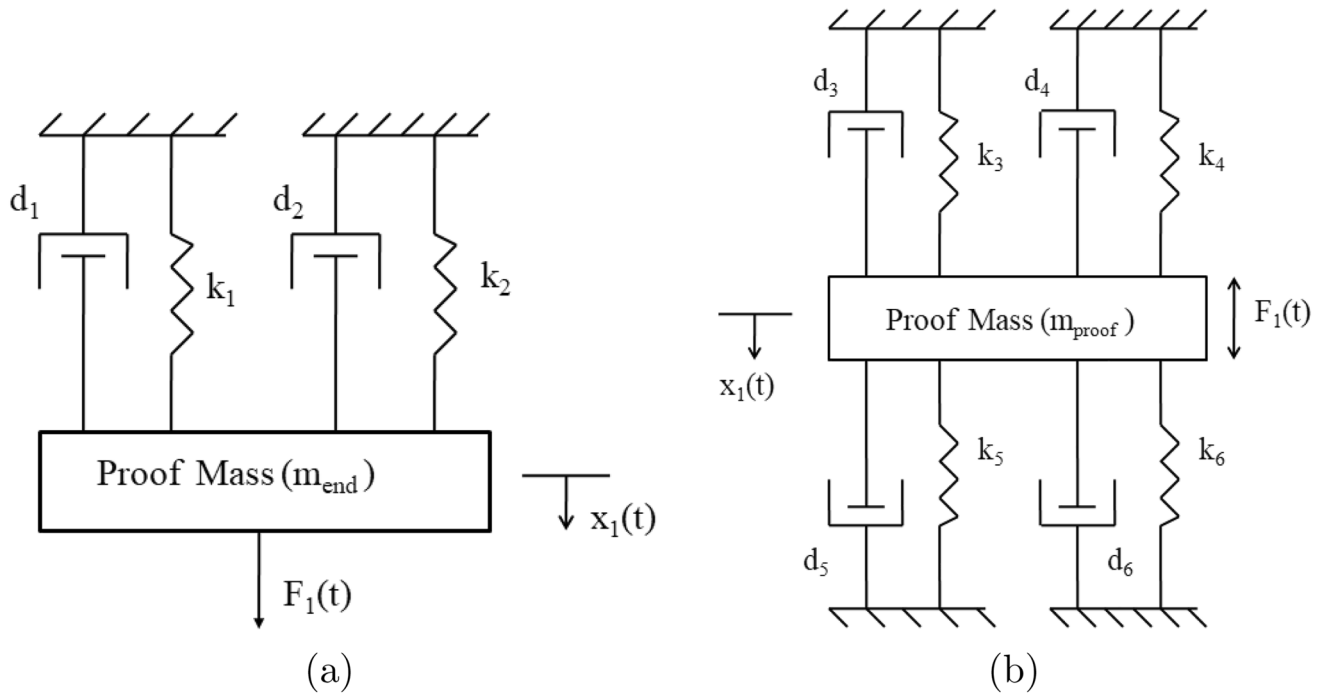


Fig. 2 Spring-mass-damper equivalent of proposed sensor **a** half-meander, **b** meander

sensitivity, optimized load resistance, and power output according to different acceleration levels are discussed in Sect. 3.3.

3.1 Stiffness study

The stiffness for both the half-meander and meander as well as corresponding conventional structures has been simulated. Table 3 represents the analytical and simulated values of different stiffness of the proposed structures. The stiffness of proposed structures along x-direction, y-direction, and z-direction can be represented as k_{xx} , k_{yy} , and k_{zz} , respectively. The stiffness of conventional-I along x-direction k_{xx} is found to be 6.56 kN/m analytically, whereas for the half-meander, it is found to be 1.60 kN/m. The simulated values of k_{xx} for conventional-I and half-meander are found to be 5.41 kN/m and 1.55 kN/m, respectively. Similarly, the k_{xx} and k_{yy} are found analytically for the meander type and conventional-II. It is observed from Table 3 that the proposed meander structures exhibit lower stiffness in comparison to conventional structures. It can also be observed from Table 3 that the simulated values of stiffness match with the analytical values.

3.2 Simulation studies: stationary analysis

3.2.1 Half-meander design

The half-meander sensor has been designed as per PiezoMUMPs process with dimensions as mentioned in Table 2. In simulation environment, the process top-down approach starts with geometry input, then material selection as per process followed by physics definition. The physics has been defined for the proposed design with taking care of different subsections which include solid mechanics, electrostatic, and electrical circuit section. In solid mechanics section, different boundary conditions as well as body load for the piezoelectric material have been defined, where the acceleration input has been given under the body load boundary condition. In electrostatic section, the boundary conditions for the charge, top terminal, and ground terminal initials have been provided for the proposed design, and in electrical circuit section, ground node as well as output load such as resistance are defined. With simulation environment, the global definitions are initially declared such as magnitude of vibration, load resistance, piezo layer, oxide layer, and structural layer dimensions with range of values as per design. Material properties of Silicon and Aluminum

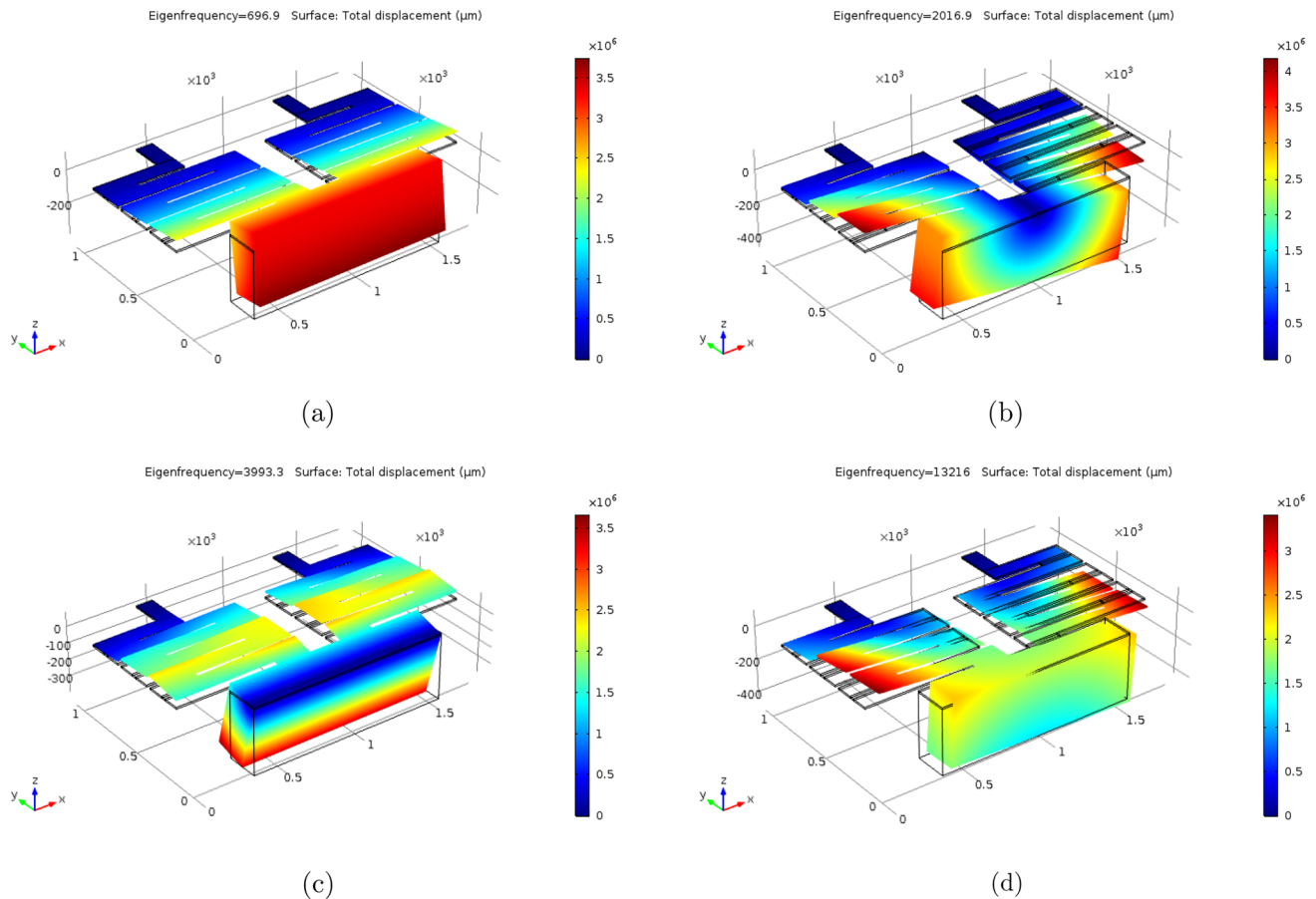


Fig. 3 Different vibration modes for half-meander structure: **a** 1st Mode, **b** 2nd Mode, **c** 3rd Mode, and **d** 4th Mode

Nitride such as density, Young's modulus, poisson's ratio, elasticity matrix, and coupling matrix are provided on the simulation environment. The body load in terms of acceleration and fixed constraint along with other boundary conditions are provided according to design for stationary as well as frequency-domain analysis. Following charge conservation principles of piezoelectric material, the electric displacement along with initial conditions is given to the proposed system, and finally, user-defined mesh is formulated with minimum element size of $0.432 \mu\text{m}$ for all the proposed designs.

As the proposed acceleration sensor utilizes *AlN* as piezoelectric material, it will be useful to explore the vibration mode, stress and strain distribution for detail characterization. Figure 3 represents different modes of vibration for half-meander architecture. The first, second, third, and fourth modes of vibration are found to be 696.9 Hz, 2016.9 Hz, 3993.3 Hz, and 13.216 kHz, respectively. The eigen frequency of

the half-meander design is computed with stationary analysis followed by frequency response analysis and the eigen response is shown in Fig. 3a. The eigen frequency for the half-meander structure is found to be 696.9 Hz. The displacement profile in the half-meander structure for different modes of vibration is represented in Fig. 3. The stress distribution profile in terms of von Mises stress for different vibration modes of half-meander design is shown in Fig. 4. The volumetric von Mises stress are found to be $9.17 \times 10^{12} \text{ Pa}$, $2.19 \times 10^{13} \text{ Pa}$, $4.52 \times 10^{13} \text{ Pa}$, and $1.012 \times 10^{14} \text{ Pa}$ for first mode, second mode, third mode, and fourth mode of vibration, respectively. The induced strain due to application of external acceleration for the half-meander and corresponding conventional structure is presented in Fig. 5. As the half-meander structure consists two-folded springs, the strain distribution has been observed for both the springs as in Fig. 1. It can be observed from Fig. 5 that the folded

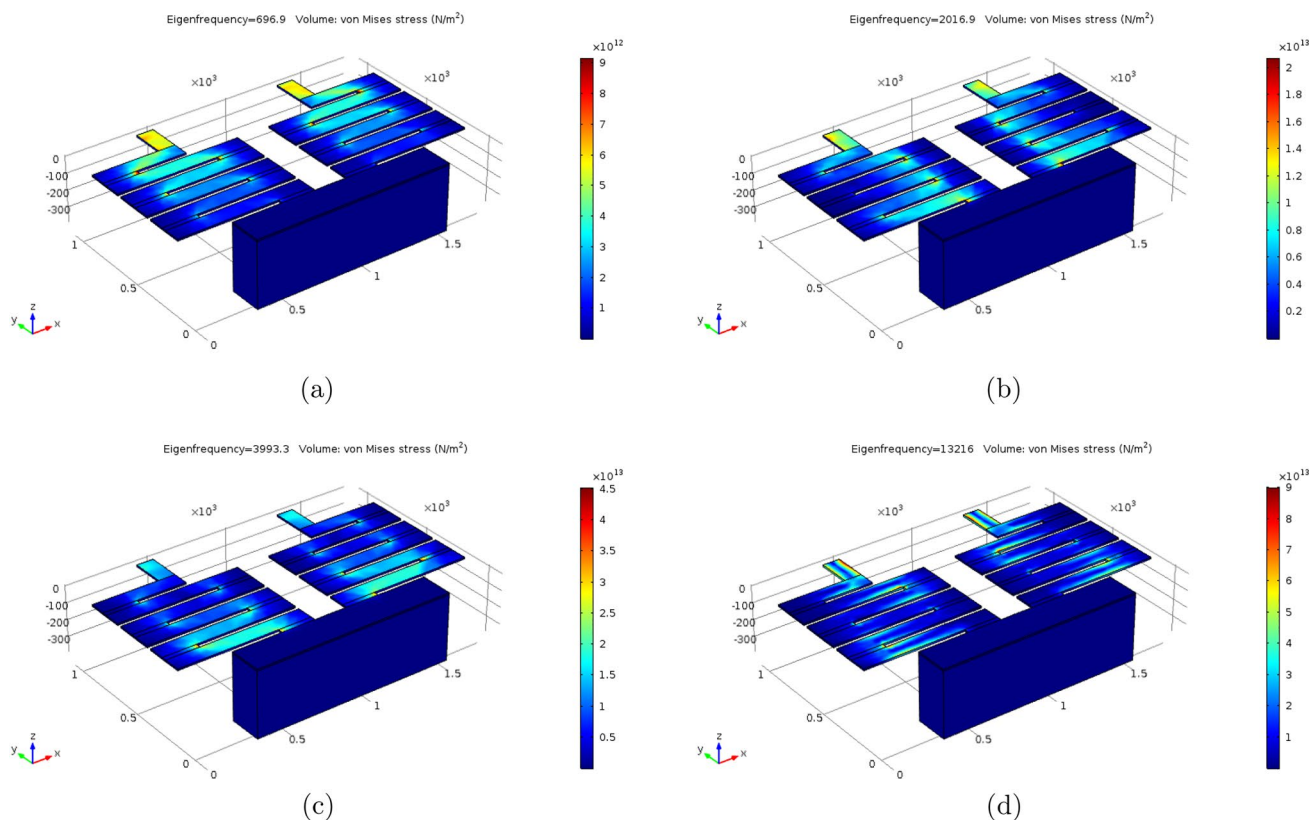


Fig. 4 Stress distribution profile for different vibration modes of half-meander structure: **a** 1st Mode, **b** 2nd Mode, **c** 3rd Mode, and **d** 4th Mode

spring in the meander architecture gives higher strain distribution in comparison to conventional. The frequency-domain behavior of half-meander structure has been discussed in Sect. 3.3.

3.2.2 Meander design

The meander sensor has been designed using finite-element analysis-based software according to *Piezo-MUMPs* process as per dimension mentioned in Table 2. The process in COMSOL has been followed as similar to half-meander design, which involves eigen frequency analysis followed frequency-domain analysis. The different vibration modes for the meander architecture is shown in Fig. 6. The first mode, second mode, third mode, and fourth mode of vibration frequencies are found to be 2.08 kHz, 2.76 kHz, 5.27 kHz, and 15.46 kHz, respectively. The displacement and stress profile for meander acceleration sensor with respect to vibration modes are presented in Fig. 6 and Fig. 7, respectively. It can be observed from Fig. 7 that

the folded spring region experiences higher amount of stress, and thus, it can contribute higher amount of charge for sensing as well as harvesting purpose. The volumetric von Mises stress for first mode, second mode, third mode, and fourth mode of vibration are found to be 1.89×10^{13} Pa, 2.22×10^{13} Pa, 5.08×10^{13} Pa, and 6.23×10^{13} Pa, respectively. The meander architecture experiences strain due to application of external acceleration. The strain profile of meander architecture with respect to its conventional geometrical design is illustrated in Fig. 8. The corrugated springs in both the meander architecture provide higher average first principal strain than the conventional one and also the spikes in the strain profile dominate the voltage producing capability in the meander design.

3.3 Simulation studies: frequency-domain analysis

The frequency-domain behavior of half-meander and meander design has been discussed with taking

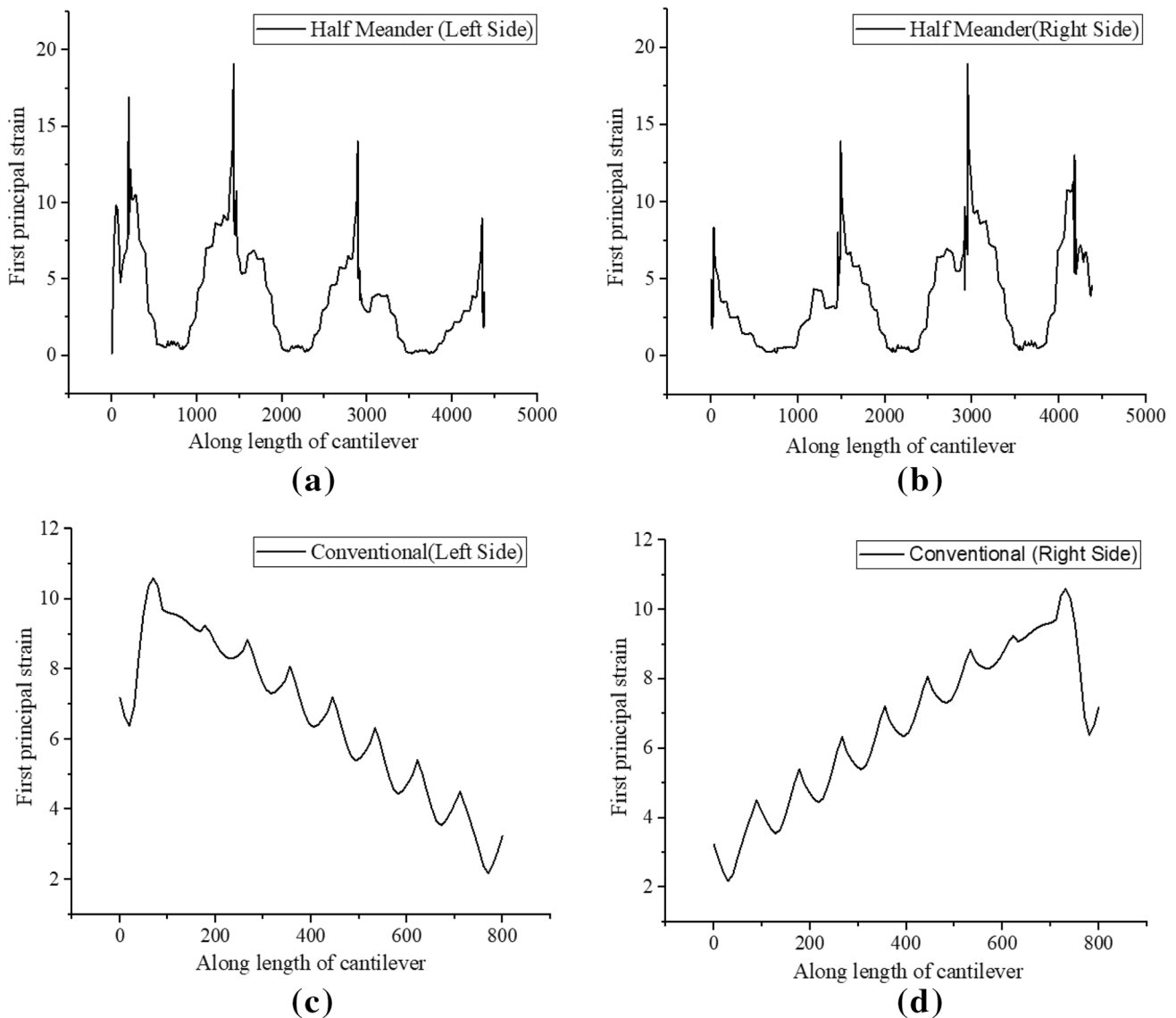


Fig. 5 Strain profile **a** Half-meander: left side spring, **b** Half-meander: right side spring, **c** Conventional: left side spring, and **d** conventional: right side spring

account of output voltage response, energy-harvesting capability in both out-of-plane and in-plane vibration direction. The proposed sensor has been characterized as acceleration sensor as well as piezoelectric energy harvester. The sensor can also be utilized in both resonant and non-resonant region due to its flat response in some frequency band. The frequency response and input–output relationship are studied using parametric analysis, where the frequency is varied with step size of 0.2 Hz and acceleration level is varied with step size of 0.1 g under study setting of simulation environment.

3.3.1 Half-meander design

In frequency response analysis, the sensor is capable of producing 3.92 V at acceleration input of 1 g in out-of-plane direction (z-axis) with resonant frequency of 696.9 Hz, which gives voltage sensitivity of 3.92 V/g and the frequency response is shown in Fig. 9a With application of 1 g acceleration in in-plane direction (y-axis), the sensor is able to generate 368 mV at load resistance of 1 MΩ. The voltage sensitivity in in-plane direction is, thus, 368 mV/g at the resonant frequency. The input–output relationship

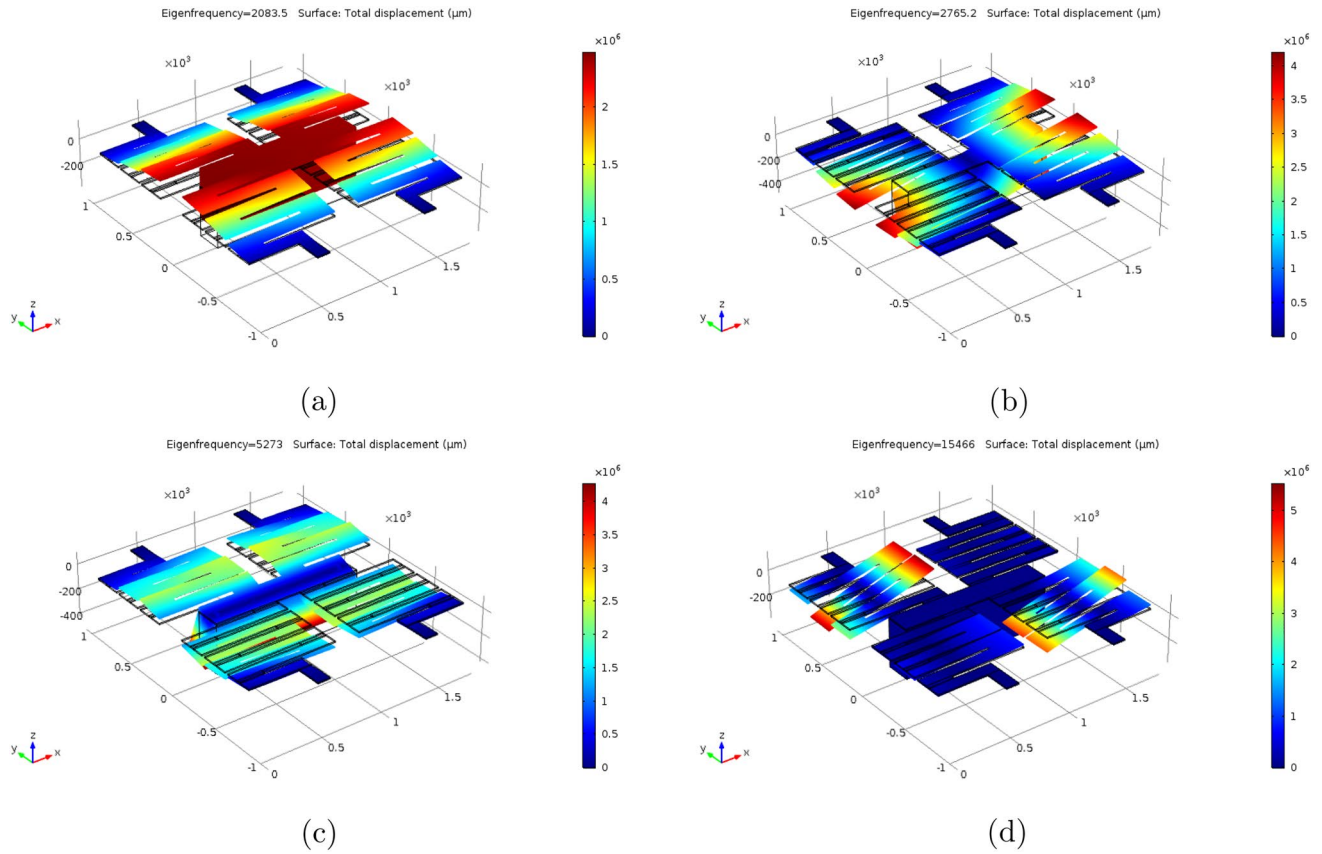


Fig. 6 Different vibration modes for meander structure: **a** 1st Mode, **b** 2nd Mode, **c** 3rd Mode, and **d** 4th Mode

(acceleration vs. output voltage) in resonant band is observed at different acceleration input levels starting from 1 g to 10 g and corresponding graph is presented in Fig. 10. It can be observed from Fig. 10a that the response and input of the sensor exhibit a linear relationship. The charge sensitivity is found to be 900 pC/g. It is observed from Fig. 9a that the sensor can also operate on range of frequencies between 200 Hz to 500 Hz at sensitivity of 1.86 mV/g to 2.07 mV/g in non-resonant region. At 500 Hz, the acceleration is varied from 0.5g to 3g to obtain the sensitivity. The slope is found to be 2, which defines the sensitivity of half-meander is 2 mV/g in non-resonant application and the corresponding graph is shown in Fig. 9c. In addition to the acceleration measurement scenario, the sensor is also capable of energy harvesting as it uses AlN piezoelectric material. The power vs. load resistance for half-meander acceleration sensor is presented in Fig. 11. The half-meander architecture produces 8 μW amount of power at 1g acceleration across the optimized load resistance of 1.8 MΩ, whereas its corresponding conventional

structure is capable of producing 2.15 μW at optimized load resistance of 560 kΩ as mentioned in Table 4.

3.3.2 Meander design

The resonant frequency for meander structure is found to be 2.08 kHz, and the frequency response is shown in Fig. 9b. The sensor is capable of producing output voltage 1.8 V at the resonant frequency in response to 1 g acceleration input. It has been observed from Fig. 10b that the output voltage increases linearly with increase in magnitude of external acceleration. The meander architecture has a voltage sensitivity of 1.8 V/g in out-of-plane direction. With the external acceleration of 1 g along the in-plane direction (y-direction), the sensor is only capable of producing the output voltage of 5 mV at the resonant frequency. Hence, there is a trade-off between the voltage sensitivity and structural stability for both the sensor. Although the voltage sensitivity of meander type is less in comparison to half-meander

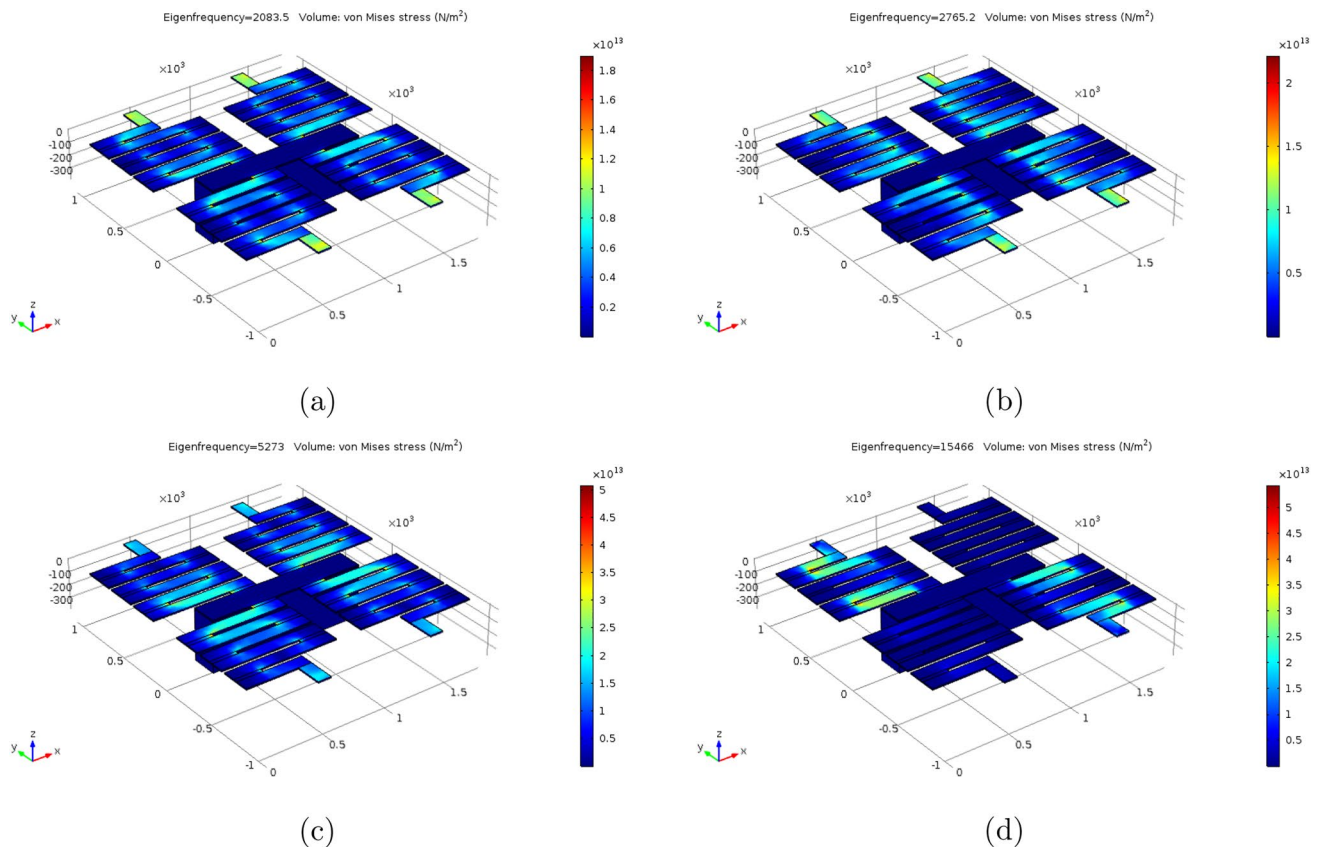


Fig. 7 Stress distribution profile for different vibration modes of meander structure: **a** 1st Mode, **b** 2nd Mode, **c** 3rd Mode, and **d** 4th Mode

design, the meander design is more reliable and stable in structure wise. The meander architecture has charge sensitivity of 143 pC/g in comparison to charge sensitivity of 4.65 pC/g of its corresponding conventional design.

The meander sensor can also operate in non-resonant region in frequency range of 1500 Hz to 1900 Hz with sensitivity of 4.57 mV/g to 4.89 mV/g . To verify the application of meander sensor in non-resonant application, the input acceleration is varied from 0.5 g to 3 g at 1545 Hz , and the slope is found to be 4.69 . Thus, the sensitivity of the meander is found to be 4.69 mV/g in non-resonant application.

The meander architecture can also be utilized for energy-harvesting prospective. The power vs. load resistance for the meander structure is illustrated in Fig. 11. It is capable of producing the power amounting of $6.35 \text{ }\mu\text{W}$ at optimized load resistance of $100 \text{ k}\Omega$ with application of 1 g acceleration input whereas its

corresponding conventional design (conventional-II) produces only $0.025 \text{ }\mu\text{W}$ at load resistance of $750 \text{ k}\Omega$. It can be observed from Table 4 that the meander architecture has less sensitivity in terms of voltage and charge sensitivity in comparison to half-meander design. Although meander design have more active piezoelectric area, the stress/ strain experienced by the half-meander springs is much more higher due to end mass placement at the free end. However, the parameters such as structural reliability, stable mechanical structural vibration in response to vibration input, longevity makes meander acceleration sensor design more suitable for said inertial measurement applications. The layout of the proposed sensor and comparison of the results are provided in Sects. 3.4 and 3.5, respectively.

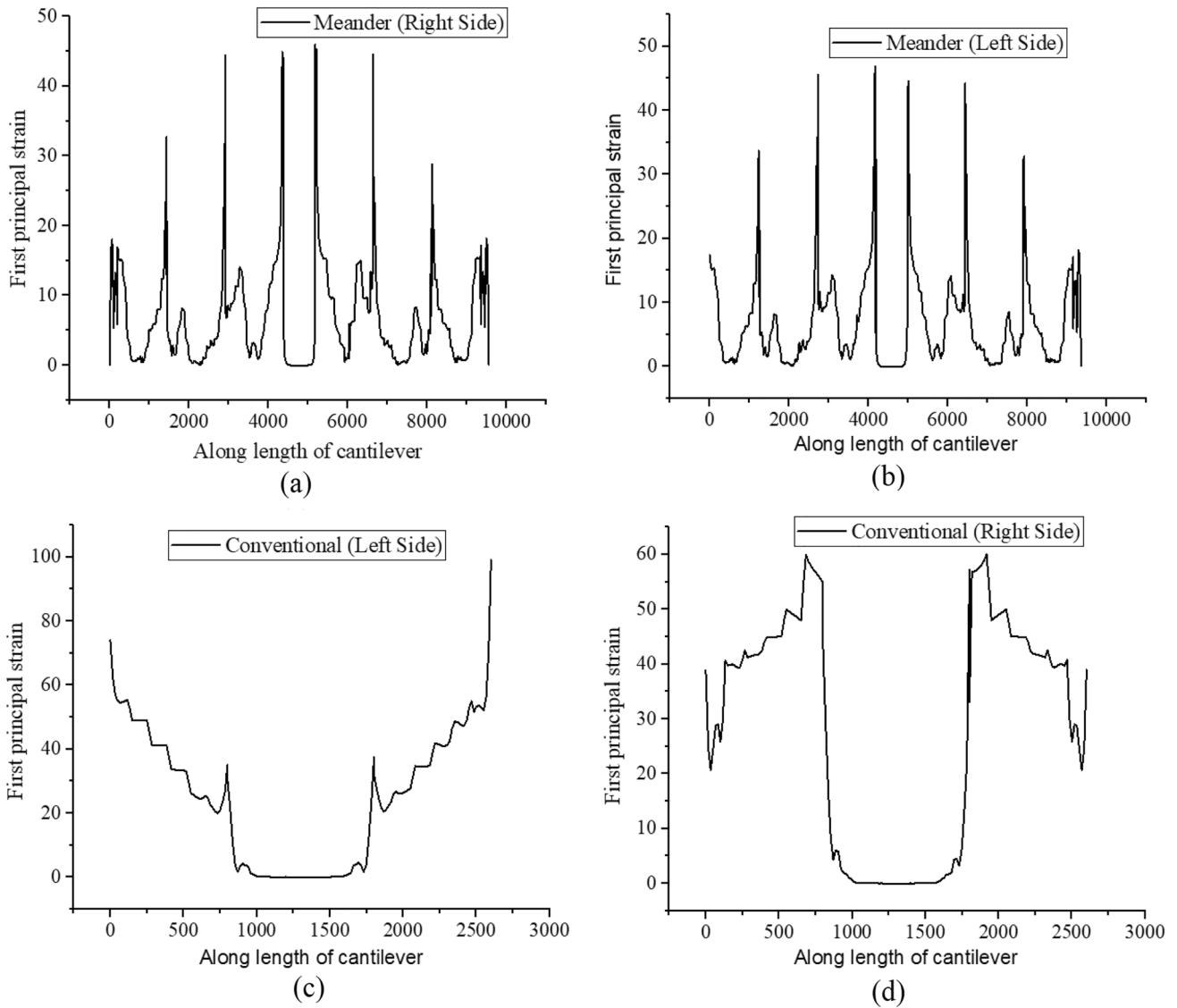


Fig. 8 Strain profile **a** meander: left side spring, **b** meander: right side spring, **c** conventional: left side spring, and **d** conventional: right side spring

3.4 Layout of proposed sensor

The layout design has been carried out for half-meander as well as meander design according to *PiezoMUMPs* guidelines governed by Cowen et. al [24]. The different layers of *PiezoMUMPs* process have been discussed in Sect. 2.1. The layout has been carried out in Tanner L-edit software by following minimum spacing between layers and boundary layers as well as minimum width of different mask layers. The layouts

of meander and half-meander acceleration sensor are represented in Fig. 12a and b, respectively.

3.5 Comparison with reported literature

The most of the reported literatures have used high volume; the designs exhibit high resonant frequency and low output voltage sensitivity; and an overview of comparison of results is presented in Table 5. In comparison to Yaghootkar et. al [20], half-meander design utilizes $1.08\text{ mm} \times 1.8\text{ mm}$ and has resonant

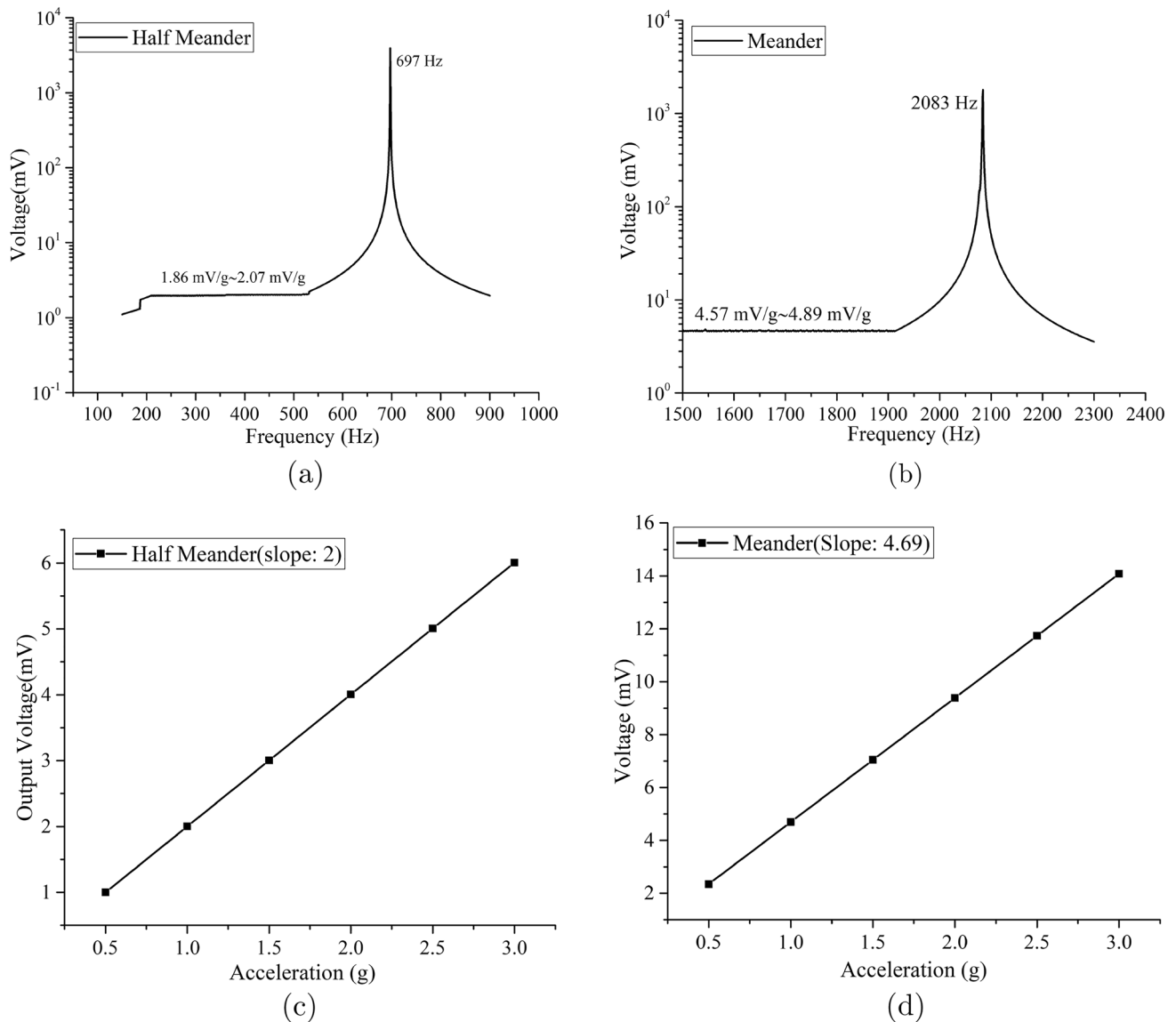


Fig. 9 Performance of sensor **a** Frequency response of Half-meander, **b** Frequency response of meander, **c** Voltage vs. acceleration, and **d** Voltage vs. acceleration

frequency approximately 697 Hz whereas their design exhibits resonant frequency of 10 kHz. The microaccelerometer designed by Xu et. al [23] exhibits high resonant frequency of 3.04 kHz and output voltage of 149.8 mV/g, whereas our both the meander designs give a better output voltage with less occupied volume. The cantilever-based piezo accelerometer reported by Xu et. al has overall device area 7 mm \times 7 mm, and resonant frequency is about 3.04 kHz, whereas our proposed half-meander and meander

exhibit less area with low resonant frequency of 696.9 Hz and 2.08 kHz.

4 Conclusion

In this work, the behavior of meander-based acceleration sensor has been studied with out-of-plane and in-plane direction of vibration. The proposed acceleration sensor can be utilized for vibration monitoring as well as measurement, and it exhibits higher voltage

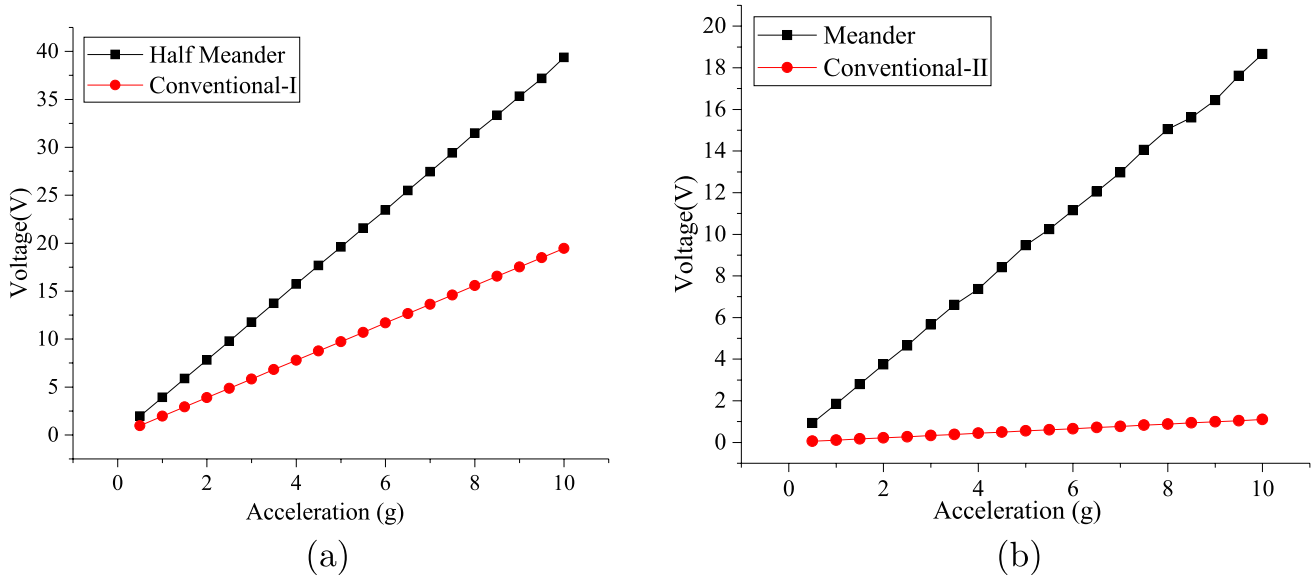


Fig. 10 Input–Output relationship (acceleration vs. voltage) of sensor at resonant region **a** conventional and half-meander, **b** conventional and meander

Table 4 Characteristics of the proposed acceleration sensor

Parameters	Conven.-I	Half-meander	Conven.-II	Meander
Resonant Frequency (<i>Hz</i>)	1069	697	3754	2083.5
Charge Sensitivity (<i>pC/g</i>)	290	900	4.65	143
Voltage Sensitivity (<i>V/g</i>)	1.94	3.92	0.11	1.8
Optimized Power (μ W)	2.15	8	0.025	6.35
Optimized $R_L(\Omega)$	560 k Ω	1.8 M Ω	750 k Ω	100 k Ω

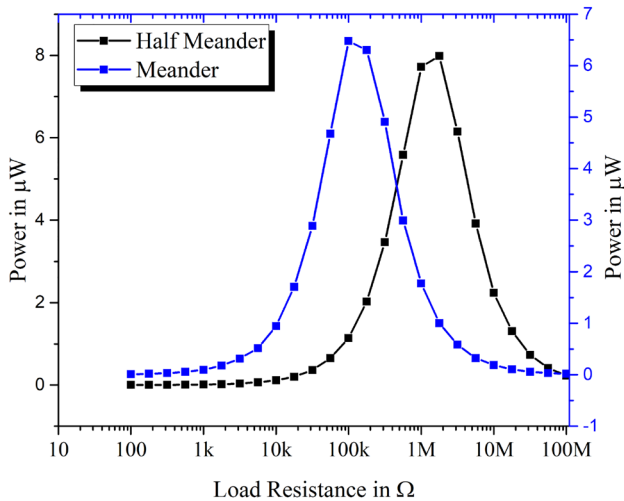
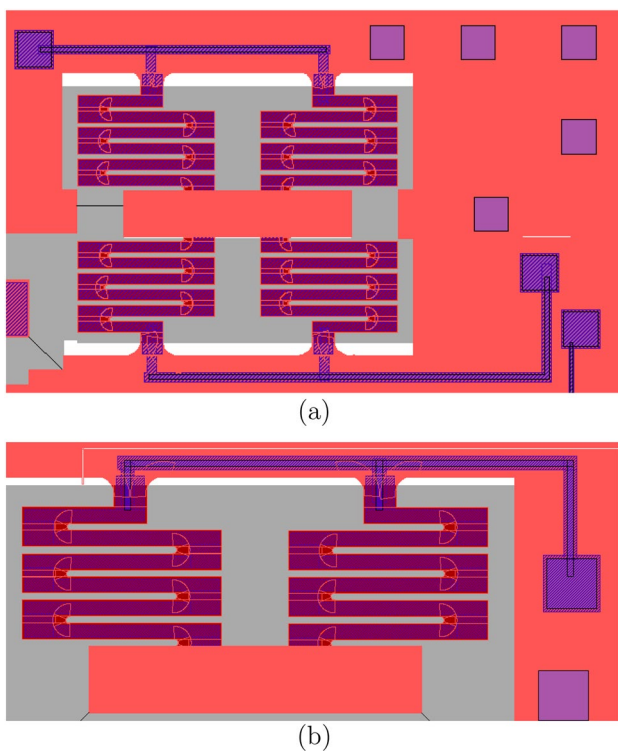


Fig. 11 Power vs. load resistance for half-meander and meander design

sensitivity as well as charge sensitivity. Moreover, both the proposed sensors occupy less volume in comparison to the literature and the resonant frequency of half-meander and meander accelerometer are observed to be 696.9 Hz and 2.08 kHz, respectively. The proposed half-meander and meander designs exhibit charge sensitivity of 900 pC/g and 143 pC/g, respectively. Also, the proposed half-meander and meander sensors have voltage sensitivity of 2 mV/g and 4.96 mV/g, respectively, for non-resonant acceleration measurement application. In resonant-based accelerometer applications, the proposed structures provide voltage sensitivity of 3.92 V/g and 1.8 V/g. The proposed sensors occupy overall area of 1.95 mm² and 3.53 mm². We have also explored the energy-harvesting capability with the meander architecture, as folded springs use piezoelectric material. The half-meander and meander sensor harvests 8 μ W and 6.35 μ W, respectively. The optimized load resistances for half-meander and meander type are found to be 1.8

Table 5 Comparison of results

Refs.	Structure	Overall area	Resonant frequency	Piezo material	Sensitivity
[20]	Membrane	5.29 mm ²	10 kHz	AlN	350 mV/g (Open circuit: 440 μV/g)
[23]	Cantilever	49 mm ²	3.04 kHz	PZT	149.8 mV/g
[28]	TWC cantilever	14.25 mm ²	1.29 kHz	ScAlN/ AlN	7.95 mV/g (400 Hz)
[29]	Cantilever	2.6 mm ²	2.19 kHz	ZnO	1.69 mV/g (500 Hz)
[13]	Membrane	63.61 mm ²	7.2 kHz	AlN	1.49 mV/g (7.2 kHz)
This Work	Half-Meander	1.95 mm ²	696.9 Hz	AlN	3.92 V/g 2 mV/g (0.2 kHz ~ 0.5 kHz)
	Meander	3.53 mm ²	2.08 kHz	AlN	1.8 V/g 4.69 mV/g (1.5 kHz ~ 1.9 kHz)

**Fig. 12** Layout of proposed sensor **a** Meander, **b** Half-Meander

MΩ and 100 kΩ, respectively. The proposed sensor can find its strong potential in the field of vibration-sensing and monitoring applications.

Acknowledgements

The authors would like to acknowledge Science and Engineering Research Board, DST, Govt. of India for funding support to this work. We also acknowledge

IIT Kharagpur for finite-element analysis simulation facility.

Author contributions

All the authors contributed the idea, technical concept, methodology, and design of proposed sensor. Simulation and mathematical analysis were done by PB. The manuscript was reviewed by SKK and BM. All authors read and approved the manuscript.

Funding

This work is funded by Science and Engineering Research Board (SERB), DST, Govt. of India under the sanction number ECR/2017/000543 to Dr. Banibrata Mukherjee.

Data availability

There are no associated datasets used in this manuscript. However, the data associated with this manuscript can be accessed upon reasonable request from the corresponding author.

Declarations

Conflict of interest The authors declare that they have no conflict of interest.

Consent to publication All authors read and approved the manuscript. The authors give consent to publication.

References

1. L. Gu, *Microelectron. J.* **42**(2), 277 (2011)
2. S.K. Kar, K.M. Swamy, B. Mukherjee, S. Sen, *IEEE Trans. Instrum. Measurement* **64**(10), 2738 (2015)
3. B. Mukherjee, K. Swamy, S. Kar, S. Sen, in *IEEE Technology Students' Symposium* (IEEE, 2011), pp. 253–258
4. S.K. Kar, K. Swamy, B. Mukherjee, S. Sen, *Microsyst. Technol.* **19**(1), 79 (2013)
5. P. Li, Z. Zhang, W. Shen, C. Hu, W. Shen, D. Zhang, *J. Mater. Chem.* **A9**(8), 4716 (2021)
6. X. Zhang, W. Wang, D. Zhang, Q. Mi, S. Yu, *J. Mater. Sci.: Mater. Electron.* **32**, 7739 (2021)
7. D. Zhang, Z. Yang, P. Li, M. Pang, Q. Xue, *Nano Energy* **65**, 103974 (2019)
8. S. Shin, A. Daruwalla, M. Gong, H. Wen, F. Ayazi, in *2019 20th International Conference on Solid-State Sensors, Actuators and Microsystems & Eurosensors XXXIII (TRANSDUCERS & EUROSENSORS XXXIII)* (IEEE, 2019), pp. 503–506
9. D. Wang, D. Zhang, P. Li, Z. Yang, Q. Mi, L. Yu, *Nano-micro Lett.* **13**, 1 (2021)
10. D. Zhang, Q. Mi, D. Wang, T. Li, *Sens. Actuators B: Chem.* **339**, 129923 (2021)
11. P. Asthana, G. Khanna, *Microelectron. J.* **93**, 104635 (2019)
12. N. Saxena, V. Sharma, R. Sharma, K.K. Sharma, K.K. Jain, *Silicon* **14**, 1–10 (2021)
13. Z.H. Chen, C.Y. Li, S.Y. Chu, C.C. Tsai, Y.H. Wang, H.Y. Kao, C.L. Wei, Y.H. Huang, P.Y. Hsiao, Y.H. Liu, *IEEE Trans. Electron Devices* **67**(10), 4399 (2020)
14. Y. Liu, B. Hu, Y. Cai, W. Liu, A. Tovstopyat, C. Sun, *Sensors* **21**(2), 453 (2021)
15. N. Gupta, A. Pandey, S.R.K. Vanjari, S. Dutta, *Microsyst. Technol.* **25**(10), 3959 (2019)
16. J. Yang, M. Zhang, Y. He, Y. Su, G. Han, C. Si, J. Ning, F. Yang, X. Wang, *Micromachines* **10**(9), 589 (2019)
17. Z. Shen, C.Y. Tan, K. Yao, L. Zhang, Y.F. Chen, *Sens. Actuators A: Phys.* **241**, 113 (2016)
18. C.C. Hindrichsen, N.S. Almind, S.H. Brodersen, R. Lou-Møller, K. Hansen, E.V. Thomsen, *J. Electroceramics* **25**(2–4), 108 (2010)
19. V. Sinatra, C. Trigona, B. Andò, S. Baglio, in *2019 IEEE International Symposium on Measurements & Networking (M & N)* (IEEE, 2019), pp. 1–5
20. B. Yaghootkar, S. Azimi, B. Bahreyni, *IEEE Sens. J.* **17**(13), 4005 (2017)
21. Y. Wang, H. Ding, X. Le, W. Wang, J. Xie, *Sens. Actuators A: Phys.* **254**, 126 (2017)
22. J. Yang, M. Zhang, C. Si, G. Han, J. Ning, F. Yang, X. Wang, *J. Microelectromech. Syst.* **28**(5), 776 (2019)
23. M.h. Xu, H. Zhou, L.h. Zhu, J.n. Shen, Y.b. Zeng, Y.j. Feng, H. Guo, *Microsyst. Technol.* **25**(12), 4465 (2019)
24. A. Cowen, G. Hames, K. Glukh, B. Hardy, *MEMSCAP Inc* **1** (2014)
25. P. Biswal, S.K. Kar, B. Mukherjee, *J. Electronic Mater.* **50**(1), 375 (2021)
26. Biswal, Priyabrata and Kar, Sougata Kumar and Mukherjee, Banibrata, in *2020 IEEE-HYDCON* (IEEE, 2020), pp. 1–5
27. O. Fedder, K. Clark, *WIT Trans. Built Environ.* **13** (1970)
28. B. Hu, Y. Liu, B. Lin, G. Wu, W. Liu, C. Sun, *IEEE Sens. J.* **21**(19), 21277 (2021)
29. C. Saayujya, J.S.Q. Tan, Y. Yuan, Y.R. Wong, H. Du, in *2014 IEEE Ninth International Conference on Intelligent Sensors, Sensor Networks and Information Processing (ISSNIP)* (IEEE, 2014), pp. 1–6

Publisher's Note Springer Nature remains neutral with regard to jurisdictional claims in published maps and institutional affiliations.

Springer Nature or its licensor (e.g. a society or other partner) holds exclusive rights to this article under a publishing agreement with the author(s) or other rightsholder(s); author self-archiving of the accepted manuscript version of this article is solely governed by the terms of such publishing agreement and applicable law.